ORIGINAL PAPER

# Isogeometric analysis of a dynamic thermo-mechanical phase-field model applied to shape memory alloys

**R. P. Dhote · H. Gomez · R. N. V. Melnik · J. Zu**

**Abstract** This paper focuses on the numerical simulation of martensitic transformations in shape memory alloys (SMAs) using a phase-field model. We developed a dynamic thermo-mechanical model for SMAs, using strain based order parameter, having a bi-directional coupling between structural and thermal physics via strain, strain rate and temperature. The model involves fourth order spatial derivatives representing a domain wall. We propose an isogeometric analysis numerical formulation for straightforward solution to the fourth order differential equations. We present microstructure evolution under different loading conditions and dynamic loading simulations of the evolved microstructures of SMAs of different geometries to illustrate the flexibility, accuracy and stability of our numerical method. The simulation results are in agreement with the numerical and experimental results from the literature.

**Keywords** Shape memory alloys · Twinning · Phase-field · Isogeometric analysis

R. P. Dhote (✉) · J. Zu
Mechanical and Industrial Engineering, University of Toronto,
5 King's College Road, Toronto, ON M5S-3G8, Canada
e-mail: rakesh.dhote@mail.utoronto.ca

H. Gomez
Department of Applied Mathematics, University of A Coruña,
Campus de Elvina, s/n., 15192 La Coruña, Spain

R. N. V. Melnik · R. P. Dhote
M²NeT Laboratory, Wilfrid Laurier University, 75 University
Avenue, Waterloo, ON N2L-3C5, Canada

R. N. V. Melnik
Universidad Carlos III de Madrid, Avenida de la Universidad 30,
E28911 Leganes, Spain

## 1 Introduction

Phase transformations are observed across different length and time scales from phase transitions due to atomic rearrangements to planet evolution. It is a widely studied phenomenon in materials science, mathematics and engineering [10,33,37,42,43]. The mathematical modeling of phase transformations involves treatment of interfaces, that is, thin transition regions, between two or more phases. Phase-field modeling is a widespread methodology where the interface is treated by a diffused smoothly-varying transition layer. The continuous treatment of interfaces reduces the problem complexity and makes its numerical approximation more tractable.

Phase-field modeling is widely used to study phase transformations in shape memory alloys (SMAs) at the meso- and nano-scale [9,31,33]. SMAs exhibit reconstructive solid-to-solid phase transformations due to symmetry breaking. The high symmetry atomic arrangement (austenite phase) is transformed into the lower symmetry arrangements (martensitic variants) from a crystallographic point of view. Phase transformations in SMAs reveal themselves as complex patterns of microstructures, such as parallel twins, zig-zag twins, cross twins, wedge and habit plane [7]. These microstructures have different phases separated by an invariant plane. A phase-field model can describe this complex microstructure by using appropriately defined conserved field variables, or order-parameters, that vary continuously across the invariant plane. A continuous variation of field variables across the invariant plane often leads to higher order differential terms in the governing equations, which poses significant challenges for the numerical discretization of the model [27].

Different numerical schemes have been proposed to solve higher-order differential equations. The finite difference method has been widely used to solve phase transformations

of SMAs on geometrically simple domains [2,35,46]. Alternatively, spectral methods have been reported to be efficient in solving phase-field models because they can resolve sharp interfaces with a moderate number of uniform grid points [11]. Other numerical techniques like the method of lines, the finite volume method or hybrid optimization algorithms have been proposed to solve phase-field models [45]. Most of the above methodologies use uniform grid stencils and are not flexible with complex geometries in real-world applications. In such scenarios, one should resort to the finite element method (FEM), which finds wide applicability across engineering disciplines to simulate physics with geometric flexibility. The FEM has been extensively used for the variational formulation of second-order differential operators, where the conforming element has inter-element continuity restricted to $\mathscr{C}^0$. However, the conforming discretization of fourth-order spatial differential operators requires the basis functions to be at least $\mathscr{C}^1$-continuous across element boundaries. There are few conforming finite elements (e.g., 2D Argyris element) which support higher order continuity, necessary for solving higher-order differential equations. One of the roundabout ways is to use mixed finite elements for spatial discretization, which leads to an increase in degrees of freedom, and, thus, is not an ideal solution. In short, there is a need of a numerical method which can have geometric flexibility and achieve higher-order continuity of the basis functions. We believe that isogeometric analysis (IGA), a recently-proposed computational method, can prove to be an effective procedure for solving higher-order problems on complex geometries.

IGA is an analysis tool based on the Non-Uniform Rational B-Spline (NURBS) basis, a backbone of modern Computer-Aided Design (CAD) packages. IGA employs complex NURBS-based representations of the geometry and the field variables in a variational formulation of the equations. Thus, IGA may open the door to technologies that directly integrate CAD and analysis, simplifying or eliminating altogether the mesh-generation bottleneck [6,13,14, 28,40,41]. Using IGA, the geometry can be modeled exactly in many instances and, as a consequence, geometric errors are eliminated. IGA accommodates the classical concepts of *h*- and *p*-refinement, but introduces a new procedure, namely *k*-refinement that seems to be unique within the geometrically flexible numerical methods. In *k*-refinement the order of the approximation is elevated, but continuity is likewise increased, creating new opportunities for the approximation of problems whose discretization requires smoothness [3– 5,16,20,24–26,29,30,38]. Thus, we believe that IGA provides unique attributes in solving higher-order differential operators with $\mathscr{C}^1$ or higher order continuity along with higher accuracy and robustness without a need of using mixed finite element formulation or non conforming elements. The accuracy and robustness of IGA methodology have been reported for solving the phase-field models in the field of crack propagation [8], spinodal decomposition [32], topology optimization [17], and tumor angiogenesis [44]. We reported the first use of the IGA for solving the phase-field models for microstructure evolution in SMAs in [18]. Here, we extend the studies to different geometries and boundary conditions, performing physically-relevant simulations (for example, tensile tests) to investigate thermo-mechanical behavior of SMA structures as a function of their microstructures.

In this paper, we model the two dimensional square-to-rectangular phase transformations in FePd SMA specimens and numerically solve the governing equations using IGA. The coupled equations of nonlinear thermoelasticity have been developed by using the phase-field model and the Ginzburg–Landau theory. The governing laws are introduced in the IGA framework by using a variational formulation that can be simply derived by multiplying the governing equations with a smooth function and integrating by parts twice. Thus, no additional variables are introduced avoiding the use of mixed methods which typically require complicated stability analyses. Using the proposed algorithm, we perform several numerical studies on SMAs under coupled thermo-mechanical dynamic loading conditions. The examples show the strong thermo-mechanical coupling of SMAs and illustrate the flexibility, accuracy and stability of our numerical methods.

The rest of the paper is organized as follows: Sect. 2 describes the derivation of the coupled thermo-mechanical model of square-to-rectangular phase transformations in SMAs. The weak formulation and IGA numerical implementation of the governing equations are described in Sect. 3. The above methodology is exemplified with several two dimensional numerical simulations on SMA patches in Sect. 4. Finally, the conclusions are given in Sect. 5.

## 2 Formulation of dynamic coupled thermo-mechanical model for square-to-rectangular phase transformations in SMAs

The square-to-rectangular phase transformations are a 2D representation of cubic-to-tetragonal phase transformations observed in several SMA materials like FePd, InTl or NiAl. The square phase represents high-temperature and high-symmetric austenite phase while rectangles, with a length along two coordinate axes, represent low-temperature low-symmetric martensite variants. The dynamics of SMA is highly dependent on the temperature. The SMA may exhibit ferroelastic, pseudo-elastic and elastic behavior at low, intermediate and high temperatures [21]. This wide range of qualitative behaviors is captured in the simulations by accounting for the coupling effects between the structural and thermal fields.

## 2.1 Theory

In this section, we derive the governing equations of SMA dynamics accounting for thermo-mechanical nonlinear coupling. We begin by introducing basic notations for the kinematics of SMAs. Let us call $\boldsymbol{u} = \{u_1, u_2\}^T$ the displacement field. We will work on the physical domain $\Omega \subset \mathbb{R}^2$, parameterized by Cartesian coordinates $\boldsymbol{x} = \{x_1, x_2\}^T$. Let us call $\boldsymbol{\epsilon}$ the Cauchy–Lagrange infinitesimal strain tensor, component-wise defined as $\epsilon_{ij} = (u_{i,j} + u_{j,i})/2$, $i, j \in \{1, 2\}$, where an inferior comma denotes partial differentiation (e.g., $u_{i,1} = \partial u_i / \partial x_1$). Let us define the following strain measures

$$e_1 = (\epsilon_{11} + \epsilon_{22})/\sqrt{2}, \quad e_2 = (\epsilon_{11} - \epsilon_{22})/\sqrt{2},$$
$$e_3 = (\epsilon_{12} + \epsilon_{21})/2, \tag{1}$$

that we call hydrostatic, deviatoric, and shear strain, respectively. To derive the fundamental equations governing the thermo-mechanical coupling of SMAs, we will use the phase-field method and Landau–Ginzburg free energy. In phase-field modeling, the different phases are distinguished using an order parameter. The order parameter for square-to-rectangular phase transformations is the deviatoric strain that we denote $e_2$. The austenite and two martensite variants are defined by $e_2 = 0$, and $e_2 = \pm 1$, respectively.

The free energy for the 2D square-to-rectangular phase-transformations considering the Landau-based potential is defined as

$$\mathscr{F} = \int_{\Omega} \left[ \frac{a_1}{2} e_1^2 + \frac{a_3}{2} e_3^2 + \frac{a_2}{2} \tau e_2^2 - \frac{a_4}{4} e_2^4 + \frac{a_6}{6} e_2^6 + \frac{k_g}{2} |\nabla e_2|^2 \right] \mathrm{d}\boldsymbol{x}$$
$$=: \int_{\Omega} F \, \mathrm{d}\boldsymbol{x} \tag{2}$$

where $a_i, k_g$ and $\theta_m$ are the material constants, $\tau = (\theta - \theta_m)/\theta_m$ is the dimensionless temperature, $\theta$ is the material temperature and $|\cdot|$ denotes the Euclidean norm of a vector living in $\mathbb{R}^2$. Figure 1 shows the plot of free-energy density $\mathscr{F}$ as a function of $e_2$ and $\theta$. When the temperature is higher than the phase transformation temperature $\theta_m$, the Landau energy function has a minimum corresponding to the austenite phase. When the temperature is lower than $\theta_m$, the energy has several minima corresponding to the variants of martensite. When the temperature is near $\theta_m$, the Landau free energy has minima corresponding to the austenite and the variants of martensite.

The kinetic energy $\mathscr{K}$, the energy associated with the external body forces $\mathscr{B}$, and the dissipation $\mathscr{D}$ are defined, respectively, as
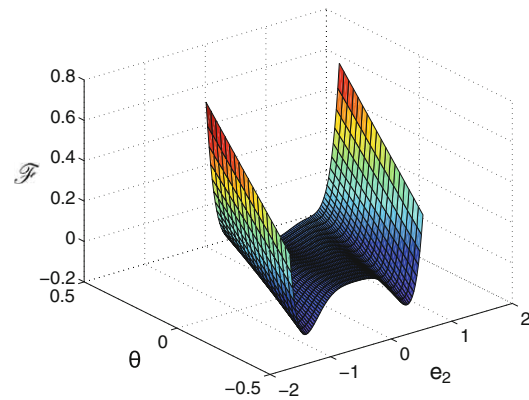


**Fig. 1** Free energy functional of square-to-rectangular phase transformations as a function of $e_2$ and $\theta$. When the temperature is higher than the phase transformation temperature $\theta_m$, the Landau energy as a function of $e_2$ has a minimum corresponding to the austenite phase. When the temperature is lower than $\theta_m$, the energy has several minima corresponding to the variants of martensite. When the temperature is near $\theta_m$, the Landau free energy has minima corresponding to the austenite and the variants of martensite (color online)

$$\mathscr{K} = \int_{\Omega} \frac{\rho}{2} |\dot{\boldsymbol{u}}| \mathrm{d}\boldsymbol{x}; \quad \mathscr{B} = \int_{\Omega} \boldsymbol{f} \cdot \boldsymbol{u} \mathrm{d}\boldsymbol{x}; \quad \mathscr{D} = \int_{\Omega} \frac{\eta}{2} \nabla \boldsymbol{u} : \nabla \boldsymbol{u} \, \mathrm{d}\boldsymbol{x},$$
$$\tag{3}$$

where $\rho$ is the density, $\boldsymbol{f}$ is the external body load vector, $\eta$ is the dissipation constant, $\dot{\boldsymbol{u}}$ indicates the time derivative of $\boldsymbol{u}$ and $\nabla \boldsymbol{u} : \nabla \boldsymbol{u} = u_{i,j} u_{i,j}$ (repeated indices indicate summation). The Hamiltonian of the problem can be expressed as

$$\mathscr{H} = \int_0^t (\mathscr{K} - \mathscr{F} - \mathscr{B} - \mathscr{D}) \mathrm{d}t$$
$$:= \int_0^t \int_{\Omega} H(t, \boldsymbol{x}, \boldsymbol{u}, \dot{\boldsymbol{u}}, \nabla \boldsymbol{u}, \nabla \nabla \boldsymbol{u}) \mathrm{d}\boldsymbol{x} \mathrm{d}t, \tag{4}$$

where $[0, t]$ is the time interval of interest. Using calculus of variations to determine the extrema of the functional (4), leads to the momentum balance equations. If we take variations with respect to $u_i$, we obtain the $i$'th component of the momentum balance equation, which is,

$$\frac{\partial H}{\partial u_i} - \frac{\partial}{\partial x_1} \left( \frac{\partial H}{\partial u_{i,1}} \right) - \frac{\partial}{\partial x_2} \left( \frac{\partial H}{\partial u_{i,2}} \right) + \frac{\partial}{\partial x_1^2} \left( \frac{\partial H}{\partial u_{i,11}} \right)$$
$$+ \frac{\partial}{\partial x_1 \partial x_2} \left( \frac{\partial H}{\partial u_{i,12}} \right) + \frac{\partial}{\partial x_2^2} \left( \frac{\partial H}{\partial u_{i,22}} \right) - \frac{\partial}{\partial t} \left( \frac{\partial H}{\partial \dot{u}_1} \right) = 0. \tag{5}$$

Equation (5) can be rewritten as

$$\rho \frac{\partial^2 u_i}{\partial t^2} = \sigma_{ij,j} + \sigma_i^g + \eta \nabla^2 \dot{u}_i + f_i, \tag{6}$$

where repeated indices indicate summation, and

$$\sigma_{11} = \frac{1}{\sqrt{2}} \left[ a_1 e_1 + a_2 \tau e_2 - a_4 e_2^3 + a_6 e_2^5 \right], \tag{7a}$$

$$\sigma_{12} = \frac{1}{2} a_3 e_3 = \sigma_{21}, \tag{7b}$$

$$\sigma_{22} = \frac{1}{\sqrt{2}} \left[ a_1 e_1 - a_2 \tau e_2 + a_4 e_2^3 - a_6 e_2^5 \right]. \tag{7c}$$

The higher-order differential term $\boldsymbol{\sigma}^g$ takes the form

$$\sigma_1^g = -\frac{k_g}{2} \left[ u_{1,1111} + u_{1,1122} \right] + \frac{k_g}{2} \left[ u_{2,1112} + u_{2,1222} \right]$$
$$= -\frac{k_g}{\sqrt{2}} \nabla^2 \left( \frac{\partial e_2}{\partial x_1} \right), \tag{8a}$$

$$\sigma_2^g = +\frac{k_g}{2} \left[ u_{1,1112} + u_{1,1222} \right] - \frac{k_g}{2} \left[ u_{2,1122} + u_{2,2222} \right]$$
$$= \frac{k_g}{\sqrt{2}} \nabla^2 \left( \frac{\partial e_2}{\partial x_2} \right). \tag{8b}$$

If we define the differential operator $\nabla^\perp$ as $\nabla^\perp = \{\partial(\cdot)/\partial x_1, -\partial(\cdot)/\partial x_2\}^T$, the stress $\boldsymbol{\sigma}^g$ can be written in divergence form as

$$\boldsymbol{\sigma}^g = \nabla \cdot \left( \frac{k_g}{2} \nabla \nabla^\perp e_2 \right).$$

To account for the thermo-mechanical coupling in this framework, we need to define an energy balance equation. We will assume that the contribution of $\boldsymbol{\sigma}^g$ to the energy balance is negligible. Under this assumption, the energy equation can be expressed as (compare with [34]):

$$\rho \frac{\partial e}{\partial t} - \boldsymbol{\sigma} : \nabla \boldsymbol{v} + \nabla \cdot \boldsymbol{q} = g, \tag{9}$$

where $\boldsymbol{v} = \dot{\boldsymbol{u}}$, $e$ is the internal energy, $\boldsymbol{q}$ is the heat flux and $g$ is the heat supply per unit mass. Following classical thermodynamics, we derive the state variables from a thermodynamic potential. Let us define the Helmholtz free energy as

$$\Psi = F - C_v \theta \ln \theta, \tag{10}$$

where $C_v$ is the specific heat of the material. In order for the theory to comply with the second law of thermodynamics, we define the internal energy and the heat flux as follows:

$$e = \Psi - \theta \frac{\partial \Psi}{\partial \theta}; \quad \boldsymbol{q} = -\kappa \nabla \theta, \tag{11}$$

where $\kappa$ is the thermal conductivity which we assume constant. Using these expressions in Eq. (9), dropping the mixed derivatives and the higher-order powers of the strains $e_i$, we obtain the following equation

$$\rho C_v \frac{\partial \theta}{\partial t} = \kappa \nabla^2 \theta + a_2 \frac{\theta}{\theta_m} e_2 \frac{\partial e_2}{\partial t} + g. \tag{12}$$

### 2.2 Strong form of the boundary-value problem for the phase-field model

Let $\Omega \subset \mathbb{R}^2$ be an open set in two dimensional space. The boundary of $\Omega$, assumed sufficiently smooth (e.g., Lipschitz), is denoted by $\Gamma$. We call $\boldsymbol{n}$ the unit outward normal to $\Gamma$. We assume the boundary $\Gamma$ to be composed of two complementary parts, such that $\Gamma = \overline{\Gamma_u \cup \Gamma_\sigma}$, $\Gamma_u \cap \Gamma_\sigma = \emptyset$. The boundary-value problem governing the dynamic evolution of the SMA can be stated as follows: find the displacements $\boldsymbol{u} : \overline{\Omega} \times (0, T) \mapsto \mathbb{R}^2$, and temperature $\theta : \overline{\Omega} \times (0, T) \mapsto \mathbb{R}$ such that

$$\rho \frac{\partial^2 \boldsymbol{u}}{\partial t^2} = \nabla \cdot \boldsymbol{\sigma} + \boldsymbol{\sigma}_g + \eta \nabla^2 \dot{\boldsymbol{u}} + \boldsymbol{f}, \quad \text{in } \Omega \times (0, T), \tag{13.1}$$

$$c_v \frac{\partial \theta}{\partial t} = \kappa \nabla^2 \theta + a_2 \theta e_2 \frac{\partial e_2}{\partial t} + g, \quad \text{in } \Omega \times (0, T), \tag{13.2}$$

$$\boldsymbol{u} = \boldsymbol{u}_D, \qquad \text{on } \Gamma_{\boldsymbol{u}} \times (0, T), \tag{13.3}$$

$$\left( \boldsymbol{\sigma} + \frac{k_g}{2} \nabla \nabla^\perp e_2 \right) \boldsymbol{n} = 0, \qquad \text{on } \Gamma_{\boldsymbol{\sigma}} \times (0, T), \tag{13.4}$$

$$\nabla \theta \cdot \boldsymbol{n} = 0, \qquad \text{on } \Gamma \times (0, T), \tag{13.5}$$

$$\boldsymbol{u}(\boldsymbol{x}, 0) = \boldsymbol{u}^0(\boldsymbol{x}), \qquad \text{in } \overline{\Omega}, \tag{13.6}$$

$$\theta(\boldsymbol{x}, 0) = \theta^0(\boldsymbol{x}), \qquad \text{in } \overline{\Omega}, \tag{13.7}$$

where $\boldsymbol{u}_D : \overline{\Omega} \mapsto \mathbb{R}^2$ denotes the prescribed displacements, and $\boldsymbol{u}_0 : \overline{\Omega} \mapsto \mathbb{R}^2$, $\theta_0 : \overline{\Omega} \mapsto \mathbb{R}$ are given functions which represent the initial displacements and temperature, respectively.

### 2.3 Dimensionless form of the phase-field equations

We rescale Eqs. (13.1) and (13.2) to a dimensionless form by using the following change of variables:

$$\begin{aligned} e_i &= e_c \bar{e}_i, & u_i &= e_c \delta \bar{u}_i, & x &= \delta \bar{x}, \\ \mathscr{F} &= \mathscr{F}_c \bar{\mathscr{F}}, & t &= t_c \bar{t}, & \theta &= \theta_c \bar{\theta}. \end{aligned} \tag{14}$$

The variables with bar and subscript $c$ are rescaled variables and constants respectively. The thermo-mechanical field Eqs. (13.1) and (13.2) can now be converted to the dimensionless form:

$$\frac{\partial^2 \bar{u}_i}{\partial \bar{t}^2} = \frac{\partial \bar{\sigma}_{ij}}{\partial \bar{x}_j} + \bar{\sigma}_i^g + \bar{\eta} \nabla^2 \dot{\bar{u}}_i + \bar{f}_i,$$

(summation on $j$ is implied) (15)

$$\frac{\partial \bar{\theta}}{\partial \bar{t}} = \bar{k} \left( \frac{\partial^2 \bar{\theta}}{\partial \bar{x}^2} + \frac{\partial^2 \bar{\theta}}{\partial \bar{y}^2} \right) + \bar{\chi} \bar{\theta} \bar{e}_2 \frac{\partial \bar{e}_2}{\partial \bar{t}} + \bar{g},$$ (16)

with rescaled constants defined as

$$e_c = \sqrt{\frac{a_4}{a_6}}, \quad \delta = \sqrt{\frac{k_g a_6}{a_4^2}}, \quad t_c = \sqrt{\frac{\rho \delta^2}{a_6 e_c^4}}, \quad \bar{\eta} = \frac{\eta t_c}{\rho \delta^2},$$

$$\bar{k} = \frac{k t_c}{\delta^2 \rho C_v}, \quad \bar{\chi} = \frac{a_2 e_2^2}{\sqrt{2} \rho C_v \theta_c}, \quad \bar{g} = \frac{g t_c}{\rho C_v \theta_c}, \bar{f}_i = \frac{f_i t_c^2}{\rho e_c \delta}.$$

(17)

## 3 Numerical formulation

We numerically implement the governing equations in a variational form utilizing IGA. We discretize the domain using $\mathscr{C}^1$-continuous functions essential for the discretization of fourth-order PDEs in primal form. The second order accurate generalized-$\alpha$ method, which accounts for high-frequency damping, is used for time integration along with an adaptive time stepping scheme developed by the authors of [23].

### 3.1 Weak formulation

The weak formulation is derived by multiplying the governing equations with weighting functions $\{U, \Theta\}$ and transforming them by using integration by parts. Initially, we consider periodic boundary conditions in all directions. Let $X$ denote both the trial solution and weighting function spaces, which are assumed to be identical. The variational formulation is stated as follows: find $S = \{u, \theta\} \in X$ such that $B(W, S) = 0 \ \forall W = \{U, \Theta\} \in X$, where

$$B(W, S) = \int_\Omega \left[ \rho U \cdot \frac{\partial^2 u}{\partial t^2} + \Theta C_v \frac{\partial \theta}{\partial t} \right] d\Omega$$

$$+ \int_\Omega \left( \nabla U : (\sigma + \eta \nabla \dot{u}) - \frac{k_g}{2} \nabla^2 U \cdot \nabla^\perp e_2 - U \cdot f \right) d\Omega$$

$$+ \int_\Omega \left[ \kappa \nabla \Theta \cdot \nabla \theta - \Theta \left( g + a_2 \frac{\theta}{\theta_m} e_2 \frac{\partial e_2}{\partial t} \right) \right] d\Omega.$$ (18)

### 3.2 Semi-discrete formulation

For the space discretization of Eq. (18), the Galerkin method is used. We approximate Eq. (18) by the following variational problem over the finite element space $X^h \subset X$. Thus, the problem can be stated as: find $S^h = \{u^h, \theta^h\} \in X^h$ such that

$$\forall W^h = \{U^h, \Theta^h\} \in X^h:$$

$$B(W^h, S^h) = 0,$$ (19)

with $W^h$ and $S^h$ defined as

$$W^h = \{U^h, \Theta^h\}, U^h = \sum_{A=1}^{n_b} U_A N_A, \Theta^h = \sum_{A=1}^{n_b} \Theta_A N_A,$$

(20.1)

$$S^h = \{u^h, \theta^h\}, u^h = \sum_{A=1}^{n_b} u_A N_A, \theta^h = \sum_{A=1}^{n_b} \theta_A N_A,$$ (20.2)

where the $N_A$'s are the basis functions, and $n_b$ is the dimension of the discrete space. In this work, we define the $N_A$'s using NURBS basis functions of degree greater than two, which achieve global $\mathscr{C}^1$-continuity or higher. A NURBS basis is constructed directly from a B-Spline basis, which is defined by using the Cox-de Boor recursion formula as [15] :

$$p = 0 : N_{i,0}(\xi) = \begin{cases} 1 & \text{if } \xi_i \leq \xi < \xi_{i+1} \\ 0 & \text{otherwise} \end{cases}$$

$$p > 0 : N_{i,p}(\xi) = \frac{\xi - \xi_i}{\xi_{i+p} - \xi_i} N_{i,p-1}(\xi)$$

$$+ \frac{\xi_{i+p+1} - \xi}{\xi_{i+p+1} - \xi_{i+1}} N_{i+1,p-1}(\xi)$$ (21)

where $p$ is polynomial order, $n$ is the number of functions in the basis, and $\xi_i \in \mathbb{R}$ is the $i$th component in a knot vector $\Xi = \{\xi_1, \xi_2, \ldots, \xi_{n+p+1}\}$. Using the B-Spline basis we can define a B-Spline curve living in $\mathbb{R}^d$ by linearly combining the basis functions as

$$F_C(\xi) = \sum_{i=1}^{n} C_i N_{i,p}(\xi),$$ (22)

with the control points $C_i \in \mathbb{R}^d$, $i \in \{1, \ldots, n\}$. A NURBS curve in $\mathbb{R}^d$ is a projective transformation of a B-Spline curve defined in $\mathbb{R}^{d+1}$. Let us assume that $D_i \in \mathbb{R}^2$, $i \in \{1, \ldots, n\}$ is a set of control points in a two-dimensional space, and let $\omega_i$ be a set of positive numbers called weights such that $\{D_i, \omega_i\} \in \mathbb{R}^3$. We define the following B-Spline curve living in $\mathbb{R}^3$ as

$$F_D(\xi) = \sum_{i=1}^{n} \{D_i, \omega_i\} N_{i,p}(\xi).$$ (23)

The NURBS curve associated to $F_D$ is defined as

$$F(\xi) = \sum_{i=1}^{n} \frac{D_i}{\omega_i} \frac{\omega_i N_{i,p}(\xi)}{\sum_{j=1}^{n} \omega_j N_{j,p}(\xi)}.$$ (24)

Note that the NURBS curve $F$ lives in $\mathbb{R}^2$. Using the notation

$$\widehat{\boldsymbol{C}}_i = \frac{\boldsymbol{D}_i}{\omega_i}, \ W(\xi) = \sum_{i=1}^{n} \omega_i N_{i,p}(\xi), \quad R_{i,p}(\xi) = \frac{\omega_i N_{i,p}(\xi)}{W(\xi)}, \tag{25}$$

we have that

$$\boldsymbol{F}(\xi) = \sum_{i=1}^{n} \widehat{\boldsymbol{C}}_i R_{i,p}(\xi). \tag{26}$$

We will call $R_{i,p}$, NURBS basis functions. Two- or three-dimensional NURBS basis can be constructed by projecting tensor products of one-dimensional B-Spline bases. We note that when there are no repeated knots in the knot vector, quadratic NURBS or B-Spline functions achieve global $\mathscr{C}^1$ continuity.

3.3 Time stepping scheme

Let $\mathbf{X}, \dot{\mathbf{X}}$, and $\ddot{\mathbf{X}}$ denote the vector of global degrees of freedom and its first, and second time derivatives, respectively. Let us define the following residual vectors:

$$\boldsymbol{R} = \{\boldsymbol{R}^C, \boldsymbol{R}^T\}^T, \tag{27.1}$$

$$\boldsymbol{R}^C = \{R_{Ai}^C\}, \tag{27.2}$$

$$R_{Ai}^C = B\left(\{N_A\boldsymbol{e}_i, 0\}, \{\boldsymbol{u}^h, \theta^h\}\right), \tag{27.3}$$

$$\boldsymbol{R}^T = \{R_A^T\}, \tag{27.4}$$

$$R_A^T = B\left(\{0, N_A\}, \{\boldsymbol{u}^h, \theta^h\}\right). \tag{27.5}$$

Given $\mathbf{X}_n, \dot{\mathbf{X}}_n$ and $\ddot{\mathbf{X}}_n$ and $\Delta t_n = t_{n+1} - t_n$, find $\mathbf{X}_{n+1}, \dot{\mathbf{X}}_{n+1}, \ddot{\mathbf{X}}_{n+1}, \dot{\mathbf{X}}_{n+\alpha_f}, \mathbf{X}_{n+\alpha_f}$, and $\ddot{\mathbf{X}}_{n+\alpha_m}$, such that

$$\boldsymbol{R}^C\left(\mathbf{X}_{n+\alpha_f}, \dot{\mathbf{X}}_{n+\alpha_f}, \ddot{\mathbf{X}}_{n+\alpha_m}\right) = 0, \tag{28.1}$$

$$\boldsymbol{R}^T\left(\mathbf{X}_{n+\alpha_f}, \dot{\mathbf{X}}_{n+\alpha_f}, \ddot{\mathbf{X}}_{n+\alpha_m}\right) = 0, \tag{28.2}$$

$$\mathbf{X}_{n+\alpha_f} = \mathbf{X}_n + \alpha_f\left(\mathbf{X}_{n+1} - \mathbf{X}_n\right), \tag{28.3}$$

$$\dot{\mathbf{X}}_{n+\alpha_f} = \dot{\mathbf{X}}_n + \alpha_f\left(\dot{\mathbf{X}}_{n+1} - \dot{\mathbf{X}}_n\right), \tag{28.4}$$

$$\ddot{\mathbf{X}}_{n+\alpha_m} = \ddot{\mathbf{X}}_n + \alpha_m\left(\ddot{\mathbf{X}}_{n+1} - \ddot{\mathbf{X}}_n\right), \tag{28.5}$$

$$\dot{\mathbf{X}}_{n+1} = \dot{\mathbf{X}}_n + \Delta t_n\left[(1-\gamma)\ddot{\mathbf{X}}_n + \gamma\ddot{\mathbf{X}}_{n+1}\right], \tag{28.6}$$

$$\mathbf{X}_{n+1} = \mathbf{X}_n + \Delta t_n\dot{\mathbf{X}}_n + \frac{(\Delta t)^2}{2}\left[(1-2\beta)\ddot{\mathbf{X}}_n + 2\beta\ddot{\mathbf{X}}_{n+1}\right]. \tag{28.7}$$

To define a second-order accurate and unconditionally stable method, the parameters $\alpha_m$ and $\alpha_f$ can be defined in terms of $\rho_\infty \in [0, 1]$, the spectral radius of the amplification matrix as $\Delta t \mapsto \infty$, as follows [15]

$$\alpha_m = \frac{1}{2}\left(\frac{3 - \rho_\infty}{1 + \rho_\infty}\right), \qquad \alpha_f = \frac{1}{1 + \rho_\infty}, \tag{29}$$

while the parameters $\gamma$ and $\beta$ must fulfill the relations

$$\gamma = \frac{1}{2} + \alpha_m - \alpha_f, \qquad \beta = \frac{1}{4}\left(1 - \alpha_f + \alpha_m\right)^2, \tag{30}$$

with choice of

$$\alpha_m \geq \alpha_f \geq \frac{1}{2},$$

for the unconditional stability.

This method can be implemented as a two-stage predictor-multicorrector algorithm as follows:

(i) Predictor stage: Set

$$\dot{\mathbf{X}}_{n+1,(0)} = \dot{\mathbf{X}}_n, \tag{31.1}$$

$$\ddot{\mathbf{X}}_{n+1,(0)} = \frac{\gamma - 1}{\gamma}\ddot{\mathbf{X}}_n, \tag{31.2}$$

$$\mathbf{X}_{n+1,(0)} = \mathbf{X}_n + \Delta t_n\dot{\mathbf{X}}_n$$
$$+ \frac{(\Delta t_n)^2}{2}\left[(1 - 2\beta)\ddot{\mathbf{X}}_n + 2\beta\ddot{\mathbf{X}}_{n+1,(0)}\right], \tag{31.3}$$

where the subscript 0 on the left-hand-side quantities is the iteration index of the nonlinear solver.

(ii) Multicorrector stage: Repeat the following steps for $i = 1, 2, \cdots, i_{max}$

1. Evaluate iterates at the $\alpha$-levels

$$\mathbf{X}_{n+\alpha_f,(i-1)} = \mathbf{X}_n + \alpha_f\left(\mathbf{X}_{n+1,(i-1)} - \mathbf{X}_n\right), \tag{32.1}$$

$$\dot{\mathbf{X}}_{n+\alpha_f,(i-1)} = \dot{\mathbf{X}}_n + \alpha_f\left(\dot{\mathbf{X}}_{n+1,(i-1)} - \dot{\mathbf{X}}_n\right), \tag{32.2}$$

$$\ddot{\mathbf{X}}_{n+\alpha_m,(i-1)} = \ddot{\mathbf{X}}_n + \alpha_m\left(\ddot{\mathbf{X}}_{n+1,(i-1)} - \ddot{\mathbf{X}}_n\right). \tag{32.3}$$

2. Use the solutions at the $\alpha$-levels to assemble the residual and the tangent matrix of the linear system

$$\boldsymbol{K}_{(i)}\Delta\ddot{\mathbf{X}}_{n+1,(i)} = -\boldsymbol{R}_{(i)}. \tag{33}$$

Solve this linear system using a preconditioned GMRES algorithm to a specified tolerance.

3. Use $\dot{\mathbf{X}}_{n+1,(i)}$ to update the iterates as

$$\ddot{\mathbf{X}}_{n+1,(i)} = \ddot{\mathbf{X}}_{n+1,(i-1)} + \Delta\ddot{\mathbf{X}}_{n+1,(i)}, \tag{34.1}$$

$$\dot{\mathbf{X}}_{n+1,(i)} = \dot{\mathbf{X}}_{n+1,(i-1)} + \gamma\Delta t_n\ddot{\mathbf{X}}_{n+1,(i)}, \tag{34.2}$$

$$\mathbf{X}_{n+1,(i)} = \mathbf{X}_{n+1,(i-1)} + \beta(\Delta t_n)^2\ddot{\mathbf{X}}_{n+1,(i)}. \tag{34.3}$$

This completes one non-linear iteration. Steps 1–3 are to be repeated until the residual vectors $\boldsymbol{R}^C$ and $\boldsymbol{R}^T$ have been reduced to a given tolerance.

The tangent matrix $\boldsymbol{K}_{(i)}$ in Eq. (33) may be computed using the chain rule as follows,

$$
\begin{aligned}
\boldsymbol{K} &= \frac{\partial \boldsymbol{R}\left(\boldsymbol{X}_{n+\alpha_f}, \dot{\boldsymbol{X}}_{n+\alpha_f}, \ddot{\boldsymbol{X}}_{n+\alpha_m}\right)}{\partial \ddot{\boldsymbol{X}}_{n+\alpha_m}} \frac{\partial \ddot{\boldsymbol{X}}_{n+\alpha_m}}{\partial \ddot{\boldsymbol{X}}_{n+1}} \\
&+ \frac{\partial \boldsymbol{R}\left(\boldsymbol{X}_{n+\alpha_f}, \dot{\boldsymbol{X}}_{n+\alpha_f}, \ddot{\boldsymbol{X}}_{n+\alpha_m}\right)}{\partial \dot{\boldsymbol{X}}_{n+\alpha_f}} \frac{\partial \dot{\boldsymbol{X}}_{n+\alpha_f}}{\partial \dot{\boldsymbol{X}}_{n+1}} \frac{\partial \dot{\boldsymbol{X}}_{n+1}}{\partial \ddot{\boldsymbol{X}}_{n+1}} \\
&+ \frac{\partial \boldsymbol{R}\left(\boldsymbol{X}_{n+\alpha_f}, \dot{\boldsymbol{X}}_{n+\alpha_f}, \ddot{\boldsymbol{X}}_{n+\alpha_m}\right)}{\partial \boldsymbol{X}_{n+\alpha_f}} \frac{\partial \boldsymbol{X}_{n+\alpha_f}}{\partial \boldsymbol{X}_{n+1}} \frac{\partial \boldsymbol{X}_{n+1}}{\partial \ddot{\boldsymbol{X}}_{n+1}} \\
&= \alpha_m \frac{\partial \boldsymbol{R}\left(\boldsymbol{X}_{n+\alpha_f}, \dot{\boldsymbol{X}}_{n+\alpha_f}, \ddot{\boldsymbol{X}}_{n+\alpha_m}\right)}{\partial \ddot{\boldsymbol{X}}_{n+\alpha_m}} \\
&+ \alpha_f \gamma \Delta t_n \frac{\partial \boldsymbol{R}\left(\boldsymbol{X}_{n+\alpha_f}, \dot{\boldsymbol{X}}_{n+\alpha_f}, \ddot{\boldsymbol{X}}_{n+\alpha_m}\right)}{\partial \dot{\boldsymbol{X}}_{n+\alpha_f}} \\
&+ \alpha_f \beta \left(\Delta t_n\right)^2 \frac{\partial \boldsymbol{R}\left(\boldsymbol{X}_{n+\alpha_f}, \dot{\boldsymbol{X}}_{n+\alpha_f}, \ddot{\boldsymbol{X}}_{n+\alpha_m}\right)}{\partial \boldsymbol{X}_{n+\alpha_f}},
\end{aligned}
\tag{35}
$$

where we have omitted the sub-index $(i)$ for notational simplicity.

## 4 Numerical simulations

To illustrate the implementation and effectiveness of the IGA approach, a number of numerical simulations have been performed using the developed dynamic thermo-mechanical model. Most numerical simulations have been performed on a rectangular SMA specimen of $\Omega = [0, L_x] \times [0, L_y]$ as shown in Fig. 2a. Moreover, some numerical simulations, in particular, on annular and circular domains, are presented to illustrate the geometrical flexibility of the approach. (refer to Fig. 2 for domain and boundary nomenclature). The initial and boundary conditions for the experiments have been described in the respective sections. The rescaling constant for spatial and temporal domain are 1.808 nm, and 1.812 ps, respectively. The $Fe_{70}Pd_{30}$ material parameters [1] used for the simulations are as described in Table 1.

In the following sections, we first validate our numerical methodology by comparing our results with those obtained by using a mixed formulation and standard $\mathscr{C}^0$ Lagrange elements. Then, we carry out the mesh refinement studies with $h$- and $k$-refinements. In all the following simulations, we use uniform knot vectors with no repeated knots. The dynamics of SMA specimens under thermo-mechanical loadings is described afterwards. Finally, we study the microstructure evolution in an annulus and circular geometry.

### 4.1 Comparison of results with Lagrange and B-Spline bases

The results of IGA have been first validated with the results from the 2D simulations carried out with the commercial Comsol Multiphysics software [12]. The mixed finite element formulation has been used to implement the thermo-mechanical equations in Comsol. The identical problems have been set up in both approaches, with same initial and boundary conditions on a square geometry with $L_x = L_y = 150$ nm. The microstructures were evolved starting from an initial displacement seed (in dimensionless unit) in the center of the domain $\boldsymbol{x}^c = \{x_1^c, x_2^c\}^T$ defined as

$$
u_1^0 = \exp(-5 \cdot 10^{-2} |\boldsymbol{x} - \boldsymbol{x}^c|^2), \qquad u_2^0 = -u_1^0,
\tag{36}
$$

starting with initial temperature $\theta^0 = 250$ K. All the boundaries of the domain have been constrained in the structural degrees of freedom $\boldsymbol{u} = \boldsymbol{0}$. The geometry is meshed
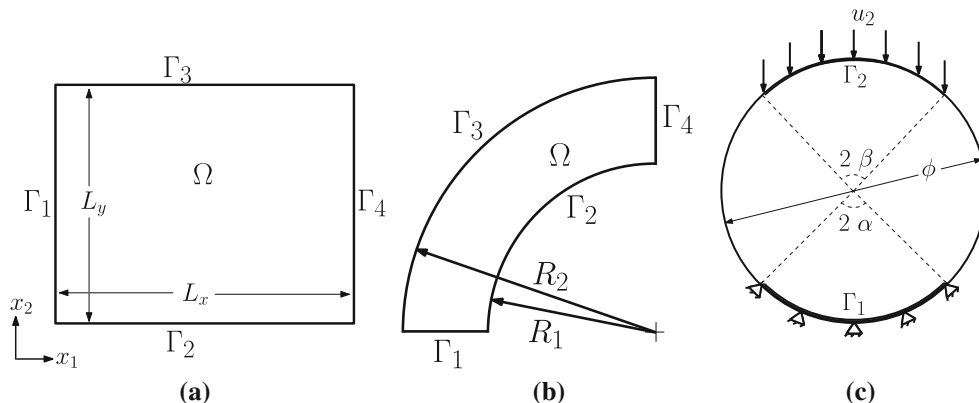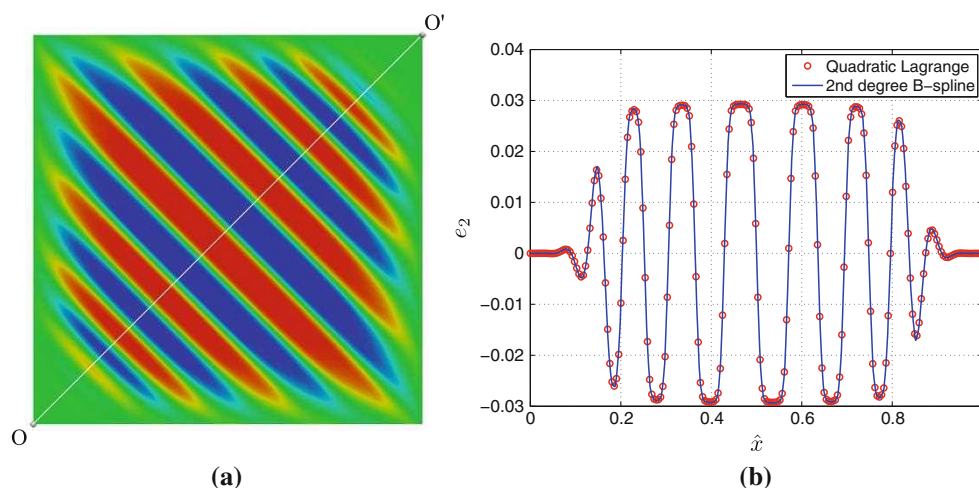


**Fig. 2** Domain and boundary nomenclature of (**a**) rectangular, (**b**) annular and (**c**) circular geometry

**Table 1** Material properties of $Fe_{70}Pd_{30}$

| $a_1$ (GPa) | $a_2$ (GPa) | $a_3$ (GPa) | $a_4$ (GPa) | $a_6$ (GPa) |
|---|---|---|---|---|
| 140 | 212 | 280 | $17 \times 10^3$ | $30 \times 10^6$ |

| $k_g$ (N) | $\theta_m$ (K) | $C_v$ ($Jkg^{-1}K^{-1}$) | $\kappa$ (W m$^{-1}$ K$^{-1}$) | $\rho$ (kg m$^{-3}$) |
|---|---|---|---|---|
| $3.15 \times 10^{-8}$ | 265 | 350 | 78 | 10,000 |



**(a)**

**(b)**

**Fig. 3** Evolved microstructure deviatoric strain $e_2$ (**a**) and cutline of $e_2$ solution for the quadratic Lagrange basis (using the Comsol Multiphysics software), and second degree B-Spline basis (using IGA) along normalized $\hat{x}$, the diagonal O–O′ (**b**) (*red* and *blue* on the left-hand-side picture indicate martensite variants and *green* indicates the austenite phase) (color online)

using $128^2$ quadratic Lagrange elements in Comsol and $130^2$ second-order $\mathscr{C}^1$-continuous B-Spline functions in the IGA. Note that using $130^2$ second-order basis functions in IGA produces $128^2$ knot spans (elements). Note also that, although the number of elements is the same in both cases, the number of global degrees of freedom is approximately 7 times smaller in the case of the IGA . We have used a constant time step of 0.25 time units in both cases. Figure 3a shows the microstructure evolution at the static equilibrium. The figures shows self-accommodated twinned microstructures. The microstructures are aligned along the diagonal of the square. The evolved microstructures are identical at the scale of the plot. We plot cut lines of the deviatoric strain order parameter $e_2$ across $\hat{x}$, the normalized diagonal O–O′, shown in Fig. 3b. The solutions have been sampled across the lines and plotted using a piecewise linear interpolation. The maximum error recorded in the results is less than 1 %. The difference in the solution in Comsol and IGA can be attributed to the different ways of implementation of the solvers. The results indicate that our implementation is correct in the IGA. The energy and average temperature evolutions during the microstructure formation using IGA are shown in Fig. 4. The results of the study show the effectiveness of IGA approach to obtain the correct solutions with far less degrees of freedom than standard Lagrange elements.

### 4.2 Mesh refinement studies

In this section, we study the sensitivity of the solution to a mesh size using the *h*- and *k*-refinements. Within the geometric flexible methods, *k*-refinement is a unique feature of the IGA that achieves better approximability increasing the order and the global continuity of the basis functions simultaneously. Our examples show how highly smooth basis functions can approximate sharp layers in the solution accurately and stably. The simulations have been carried out on the square domain with $L_x = L_y = 90$ nm using B-Splines of degree $p = 2$, $p = 3$, and $p = 4$, and global continuity $\mathscr{C}^{p-1}$. For each case, we employ meshes composed of $32^2, 64^2$, and $128^2$ elements. We use periodic boundary conditions and the same initial condition as described in Sect. 4.1.

We are interested here in microstructure evolution i.e., the spatial variation of the deviatoric strain $e_2$. The fully evolved microstructure has accommodated martenstic twins which are periodic on boundaries. The deviatoric strains are plotted at the same time instant for the coarsest mesh (second degree $32^2$ element mesh) and the finest mesh (fourth degree $128^2$ element mesh) in Fig. 5. The meshes with other basis functions approximate sharp layers accurately.

The maximum error with the coarsest mesh is less than 2 % with respect to the fine mesh indicating that with the IGA, the good results can be obtained even on the coarsest
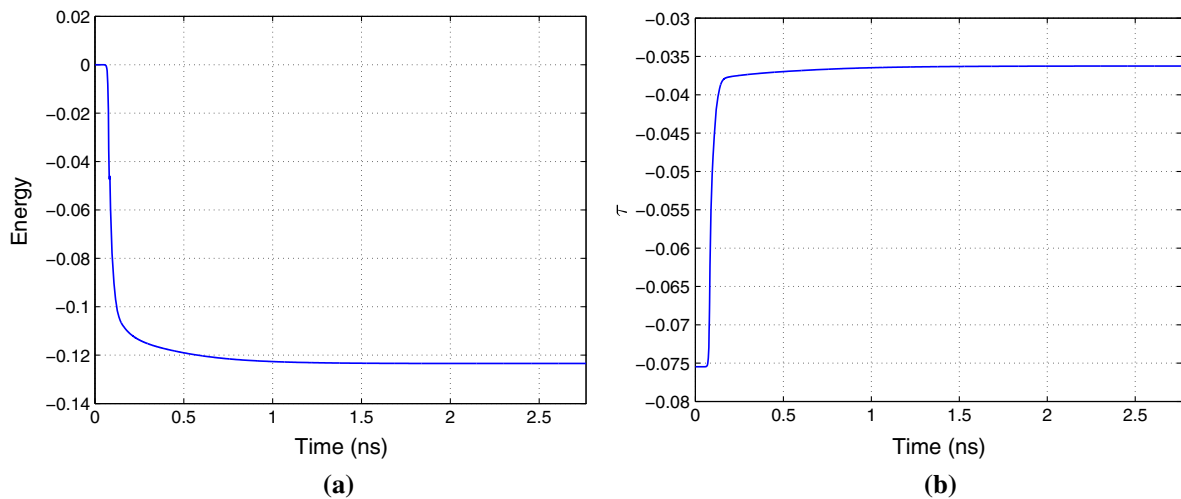
**Fig. 4** Plot of dimensionless (**a**) energy and (**b**) temperature $\tau$ evolution with time for the numerical example described in Sect. 4.1

**Fig. 5** Mesh refinement studies. The plot shows the deviatoric strain $e_2$ results for the coarsest and finest meshes (*red* and *blue* indicate martensite variants and *green* indicates the austenite phase) (color online)



(**a**) Quadratic $32^2$

(**b**) Quartic $128^2$
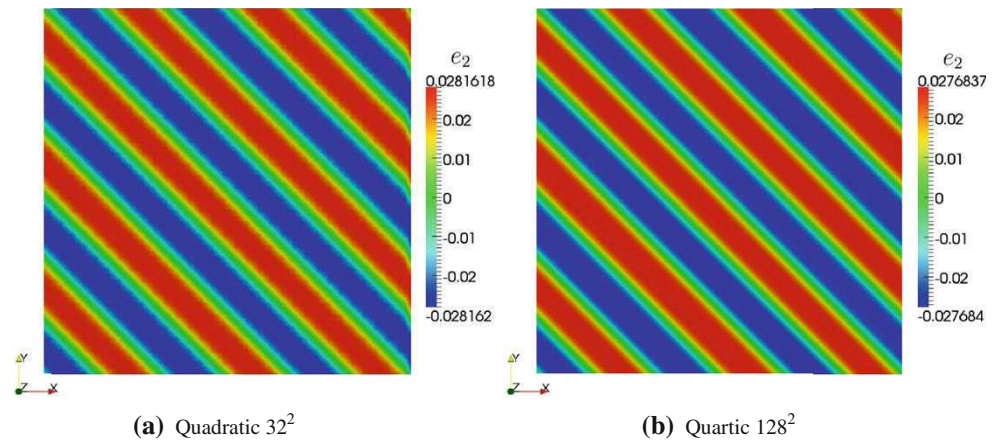
mesh. The cut line of $e_2$ and its error for meshes with 32 B-Spline basis and different continuity, with respect to the fine mesh are plotted along $\hat{x}$, the normalized diagonal O–O$'$, in Fig. 6.

### 4.3 Body and thermal loadings

To explore the importance of thermo-mechanical modeling in SMAs, we conduct a dynamic loading on a square domain with $L_x = L_y = 250$ nm. The body and thermal loads are applied in the domain as

$$\boldsymbol{f} = \boldsymbol{f}^0 \sin(\pi t/t_t), \qquad g = g^0 \sin(\pi t/t_t), \qquad (37)$$

where $\boldsymbol{f}^0$, $g^0$ are the mechanical load and thermal load acting on the body, and $t_t$ is the total time. The sinusoidal load has been applied with $f_1^0 = 0.5$, $f_2^0 = 0$, and $g^0 = -0.25$ in the dimensionless units for $t_t = 2$ ns. Three different simulations have been conducted with body load, thermal load, and combined body and thermal loads.

The microstructure evolution for three simulations are shown in Figs. 7, 8, and 9. Note that the body load acts in the

$x_1$ direction only. In the first simulation with body load, the favorable martensite variant M+ pocket, to the $f_1^0$ loading, appears at the boundary $\Gamma_1$ and accommodated martensite variant M− pocket on the opposite boundary $\Gamma_4$. The second simulation, with thermal load, favors the evolution of accommodated twinned microstructure morphology in a domain. The needle shaped twin, as also observed experimentally [39], is also captured with the developed dynamic thermo-mechanical model. The third simulation with simultaneous application of body and thermal loads causes the domain to evolve into a complex microstructure (refer to Fig. 9). The complex microstructure is a result of thermo-mechanical coupling in SMAs. The evolution of the average temperature in all three cases is shown in Fig. 10. These three simulations show the strong impact of dynamic thermo-mechanical coupling on microstructure evolution, and illustrate the necessity of using coupled thermo-mechanical theories.

### 4.4 Tensile testing

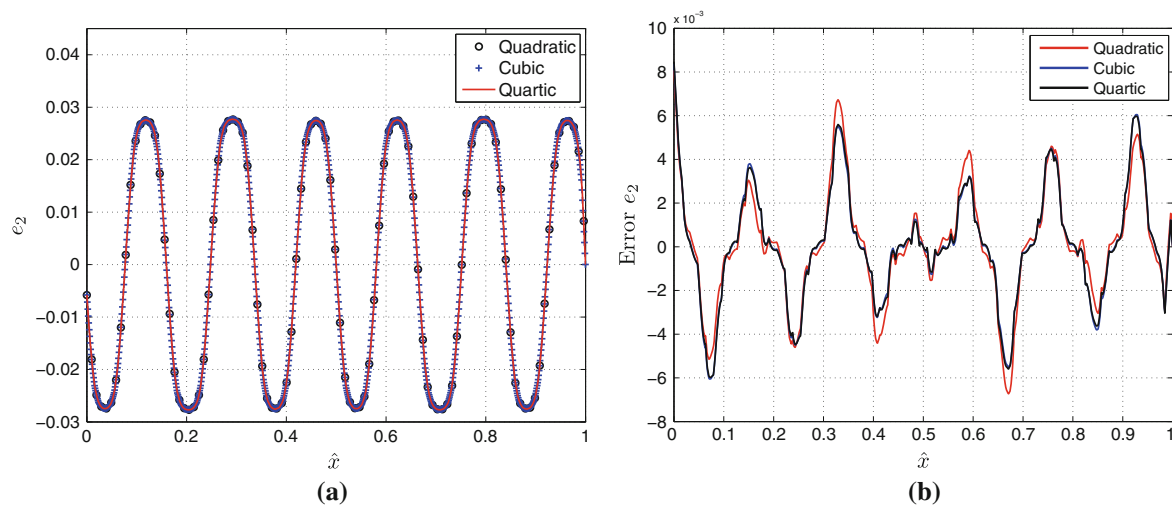To understand the thermo-mechanical properties of the microstructure, we conduct tensile tests on the SMA wire

**Fig. 6** Mesh refinement studies. Plot of cutline of the solution of **(a)** deviatoric strain, and **(b)** error with respect to finest mesh (fourth degree 128 B-Spline basis functions in each direction), along normalized $\hat{x}$, the diagonal O–O′, for 32 basis function meshes
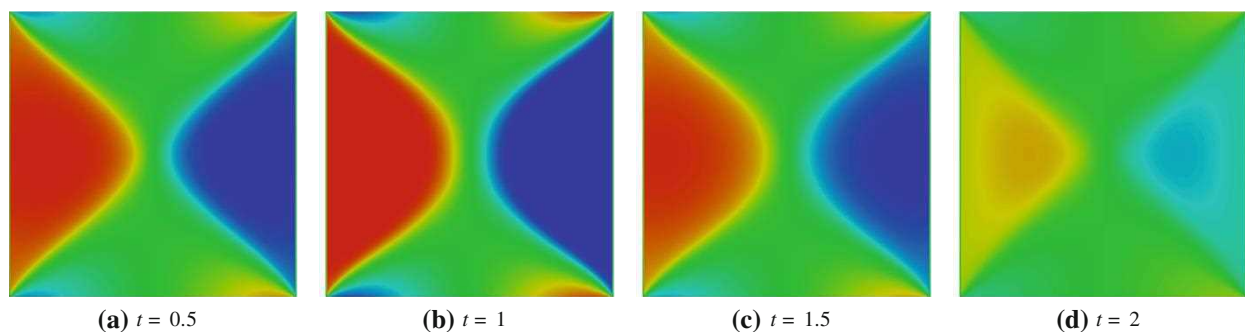


**(a)** $t = 0.5$     **(b)** $t = 1$     **(c)** $t = 1.5$     **(d)** $t = 2$

**Fig. 7** Microstructure evolution under body load at different time instants $t$ (ns) (*red* and *blue* indicate martensite variants and *green* indicates the austenite phase) (color online)



**(a)** $t = 0.5$     **(b)** $t = 1$     **(c)** $t = 1.5$     **(d)** $t = 2$
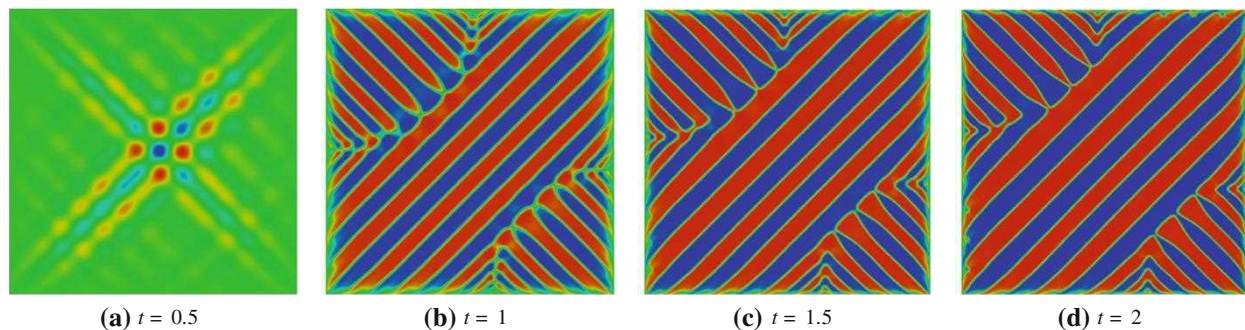
**Fig. 8** Microstructure evolution under thermal load at different time instants $t$ (ns) (red and blue indicate martensite variants and *green* indicates the austenite phase) (color online)

under dynamic loading conditions. The rectangular nanowires of domain $\Omega = [0, 1100] \times [0, 220]$ nm are dynamically loaded under three cases starting with initial temperatures 245 K (case 1), 265 K (case 2), and 285 K (case 3) corresponding to the temperatures below, equal, and above the critical temperature $\theta_m$. The nanowires, initially in austenite phase,

were first quenched at the temperatures and microstructures are allowed to evolve with constrained boundaries $\boldsymbol{u} = \boldsymbol{0}$. The nanowires are evolved to the accommodated twinned martensite phase in the case 1 and austenite in the case 2 and case 3 as shown in the subplots (a) of Figs. 11, 12, and 13. Next, tensile tests have been carried out on the evolved nanowire
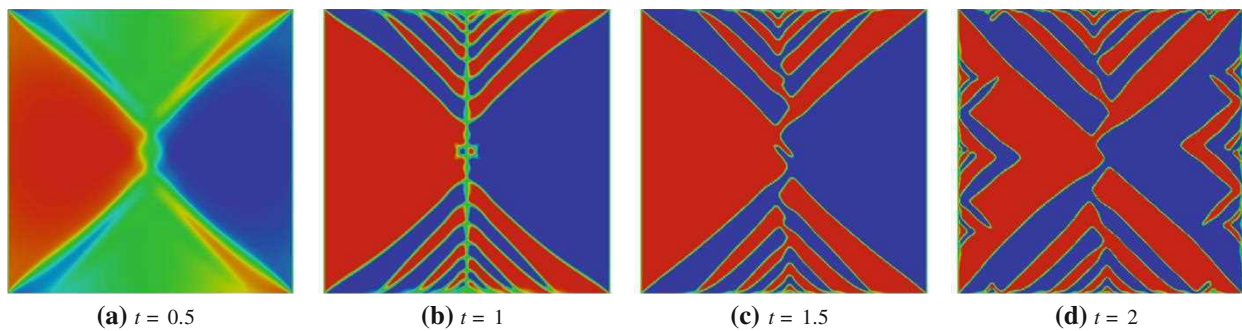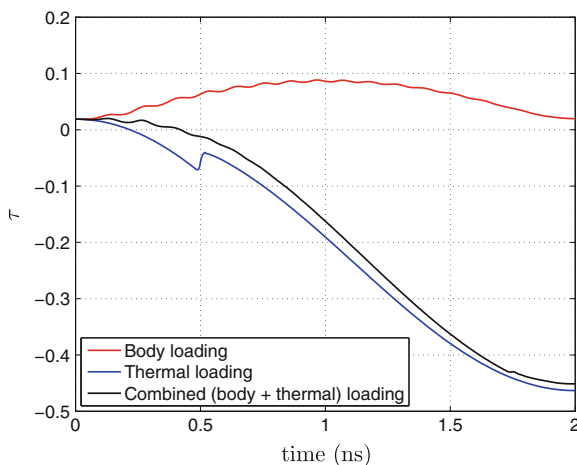
**(a)** $t = 0.5$          **(b)** $t = 1$          **(c)** $t = 1.5$          **(d)** $t = 2$

**Fig. 9** Microstructure evolution under simultaneous body and thermal loads at different time instants $t$ (ns) (*red* and *blue* indicate martensite variants and *green* indicates the austenite phase) (color online)



**Fig. 10** Average temperature $\tau$ (dimensionless) evolutions during body, thermal, and combined loadings (color online)

specimens separately. The domain is fixed on boundary $\Gamma_1$ with $\boldsymbol{u} = \boldsymbol{0}$ and ramped loading and unloading based displacements, equivalent to the strain rate of $3 \times 10^7$ s$^{-1}$, have been applied to the boundary $\Gamma_4$ in the $x_1$ direction. The high strain rate is a consequence of model rescaling.

In the case 1, the twinned microstructure is converted into the detwinned microstructure with the unfavorable martensite M$-$ converting into the favorable martensite M$+$. In the case 2 and case 3, the austenite is converted into the detwinned martensite by the movement of habit plane. Figure 14 shows the average axial stress-strain and average temperature evolution of the three cases. The significant influence of dynamic loading is observed in the average temperature evolution due to bi-directional coupling of $e_2$, $\dot{e}_2$, and $\theta$. The phase transformation takes place simultaneously along with the elastic loading under the influence of high strain rate. Due to the loading in the cases 2 and 3, the austenite is converted into the favorable M$+$ variant causing habit plane to form. The stress-strain curve is stiffer in the case 2 and 3 due to the higher stiffness of austenite phase of SMAs at higher temperature. These observations are in agreement with the earlier

published results based on the mixed formulation, as well as on the experimental observations of SMAs under high strain loading [19,22,36].

### 4.5 Loading an annulus geometry

In the earlier sections, we conducted the studies on square and rectangular domains. Here we conduct the dynamic loading studies on the annulus geometries. The strength of IGA is to model complex geometry exactly, thus eliminating geometrical errors. The quarter annulus geometry domain $\Omega$ is modeled as shown in Fig. 2b, with $R_1 = 375$ nm and $R_2 = 500$ nm. The domain is meshed with 64, and 256 quadratic $\mathscr{C}^1$-continuous NURBS based elements along radial, and circumferential directions, respectively.

Two sets of simulations have been carried out in two stages each. In the first stage, boundaries $\Gamma$ were fixed and microstructure was allowed to evolve at 240 K (case 1) and 275 K (case 2), below and above the transition temperature starting with a random initial condition. The evolved microstructures in both cases are shown in subplots (a) in Figs. 15 and 16. The domain evolves into an accommodated microstructure in case 1. It is observed that the width of martensitic twins are not uniform in the center of the domain, which is distinct from the uniform spacing of martensitic twins in a rectangular domain in Sect. 4.4 (refer to Fig. 11a). In the case 2, the domain remains in an austenitic phase.

In the second stage, the evolved annulus domain is fixed along the boundary $\Gamma_1$ with $\boldsymbol{u} = \boldsymbol{0}$ and ramped loading and unloading based displacements, equivalent to the strain rate of $3 \times 10^7$ s$^{-1}$, have been applied to the boundary $\Gamma_4$ in the direction $x_1$. In the case 1, the phase transformation starts at the loading boundary $\Gamma_4$. The detwinned microstructure is converted into the favorable M$+$ phase through the process of detwinning during loading, as observed in Fig. 15a–d. At the end of loading (refer to subplot (e)), the annular domain has M$+$ and M$-$ and traces of unconverted detwinned martensite. The microstructure at the end of the unloading is presented in the subplot (f).
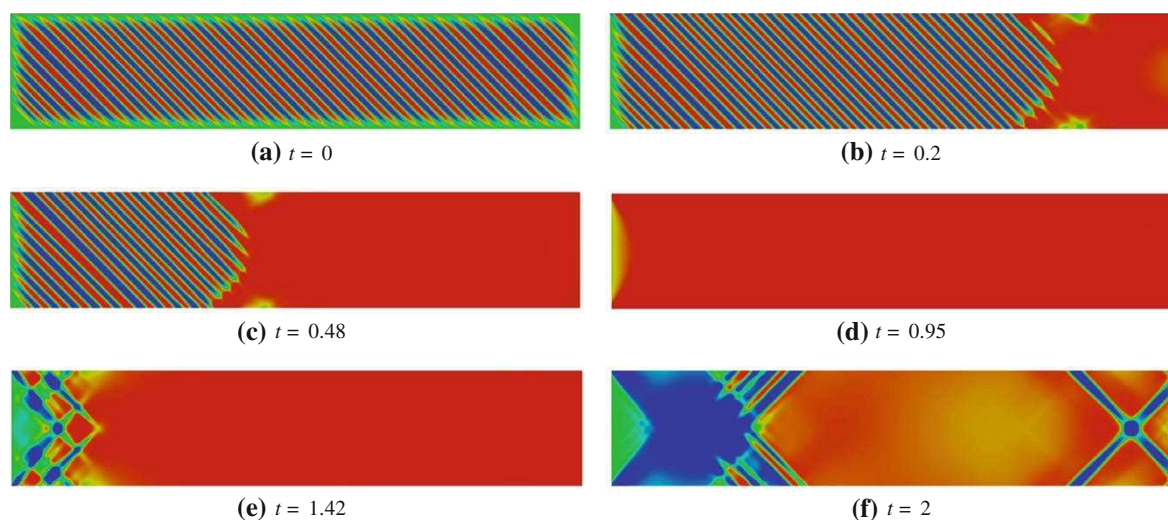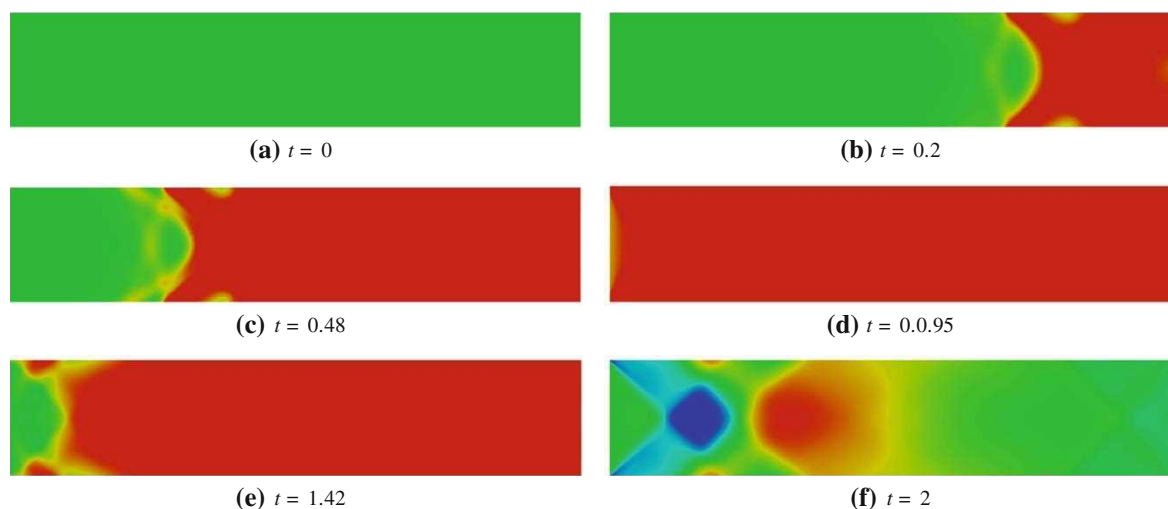
**Fig. 11** Microstructure evolution in nanowire during loading and unloading at different times $t$ (ns) for case 1 (*red* and *blue* indicate martensite variants and *green* indicates the austenite phase) (color online)



**Fig. 12** Microstructure evolution in nanowire during loading and unloading at different times $t$ (ns) for case 2 (*red* and *blue* indicate martensite variants and *green* indicates the austenite phase) (color online)

The second stage of simulation in case 2 is presented in Fig. 16. During a loading cycle, the movement of the habit plane causes the austenite to get converted into the M+ favorable phase as observed in the subplot (b). As the phase transformation progresses rearrangements of microstructures are observed in the subplots (c–e). The microstructure at the end of the unloading is presented in the subplot (f). The average temperature evolutions for both simulations are plotted in Fig. 18a.

### 4.6 Loading a circular geometry

Finally, we conduct a loading simulation on a SMA circular domain. The circular domain $\Omega$, as shown in Fig. 2c, is

constrained at the bottom boundary $\Gamma_1$ and loaded at the top boundary $\Gamma_2$. The arc lengths of $\Gamma_1$ and $\Gamma_2$ are chosen as $2\alpha = 2\beta = \pi/2$ radians. A simulation has been carried out by loading the domain with a ramp displacement $\boldsymbol{u}$ equivalent to the strain rate of $3 \times 10^7 \, \mathrm{s}^{-1}$ for 1 ns in the negative $x_2$ direction. The initial conditions used are $\boldsymbol{u} = \boldsymbol{0}$ and $\theta_0 = 240$ K.

The microstructure evolution is as shown in Fig. 17. The phase transformation starts at the $\Gamma_2$ boundary and propagates as a habit plane between twinned martensites, aligned along $\pm\pi/4$ about the vertical central line of the circular geometry, and an austenite domain as shown in a subplot (a). As the phase transformation progresses (refer to subplot (b)), the whole domain is converted into a complex microstructure, with twins of different widths and small pockets of martensitic variants in dots like microstructures, in a sector defined
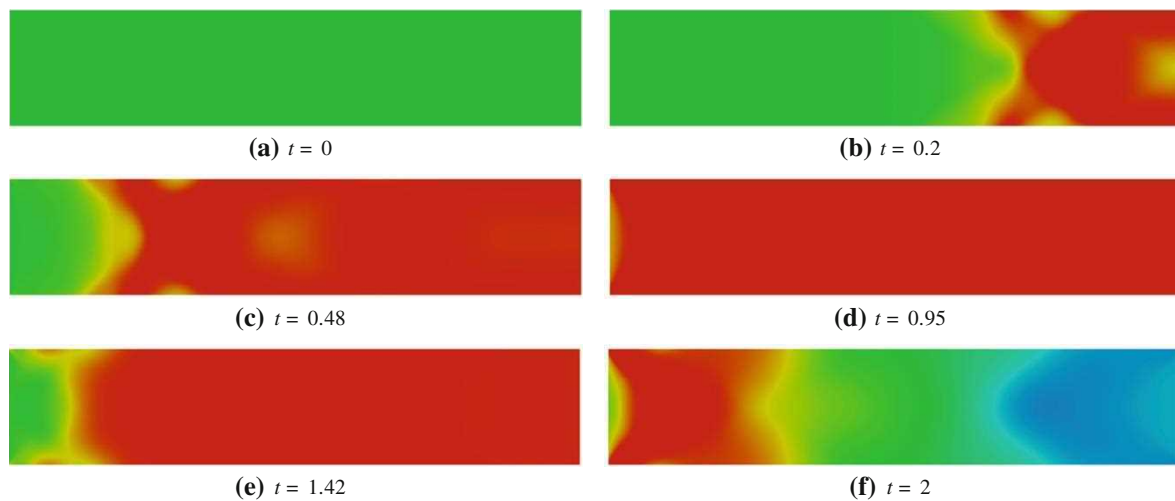
**Fig. 13** Microstructure evolution in nanowire during loading and unloading at different times $t$ (ns) for case 3 (*red* and *blue* indicate martensite variants and *green* indicates the austenite phase) (color online)
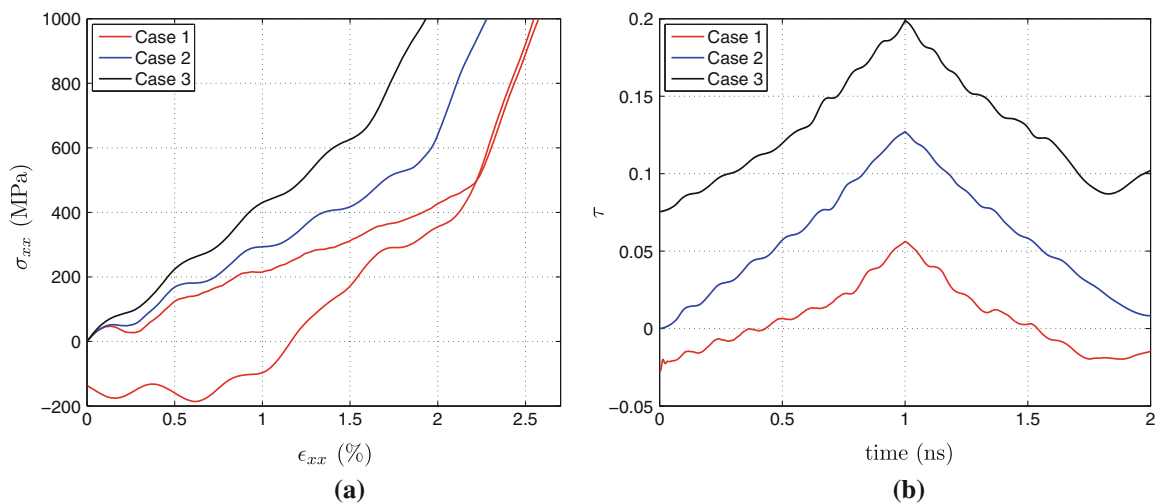


**Fig. 14** Evolution of average (**a**) axial stress–strain and (**b**) dimensionless temperature $\tau$ in the nanowire specimens for three cases (color online)
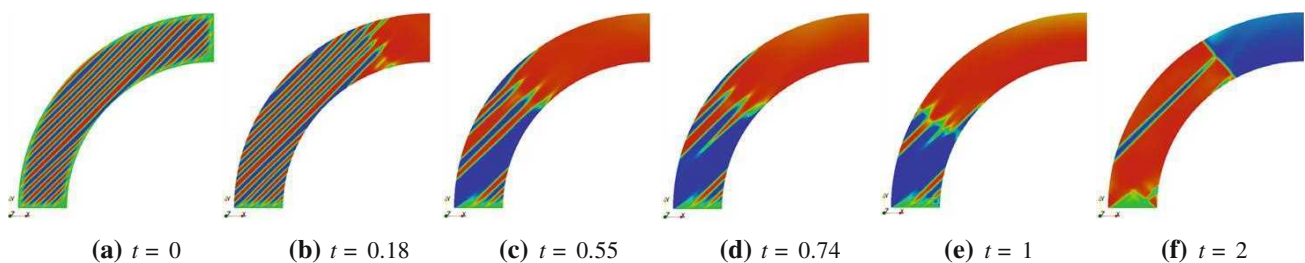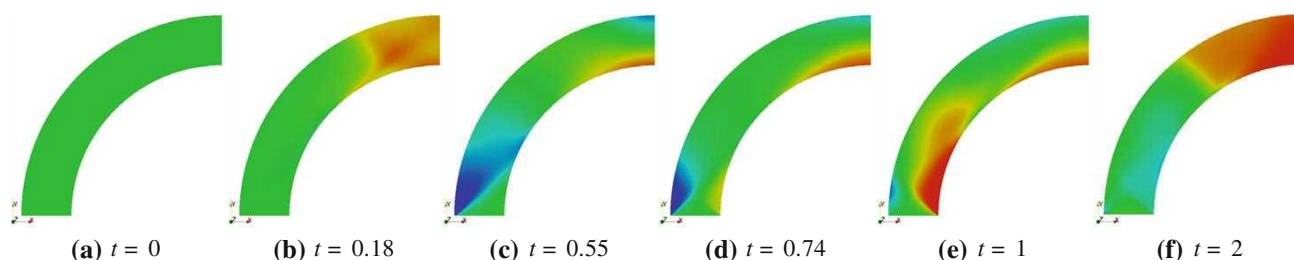


**Fig. 15** Microstructure evolution in an annulus domain at different times $t$ (ns) on loading for case 1 (*red* and *blue* indicate martensite variants and *green* indicates the austenite phase) (color online)

by $2\alpha$, in Fig. 2c. Further, the partially developed microstructures evolve into twins and start to coalesce as seen in subplots (c–d). At the end of the loading, as shown in a subplot (e), the twins span till the vertical central line of the circular geometry. The top sector, described by the sector $2\beta$, is converted into the M+ martensite. It is to be noted that there exist traces of austenite at $\Gamma_1$, due to the constrained boundary conditions. The average temperature evolution is plotted in Fig. 18b.

**Fig. 16** Microstructure evolution in an annulus domain at different times *t* (ns) on loading for case 2 (*red* and *blue* indicate martensite variants and *green* indicates the austenite phase) (color online)
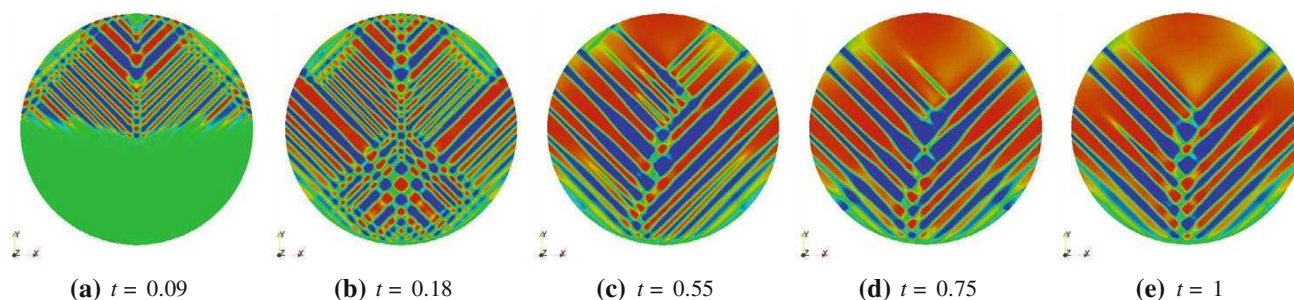


**Fig. 17** Microstructure evolution in a circular domain at different times *t* (ns) (*red* and *blue* indicate martensite variants and *green* indicates the austenite phase) (color online)
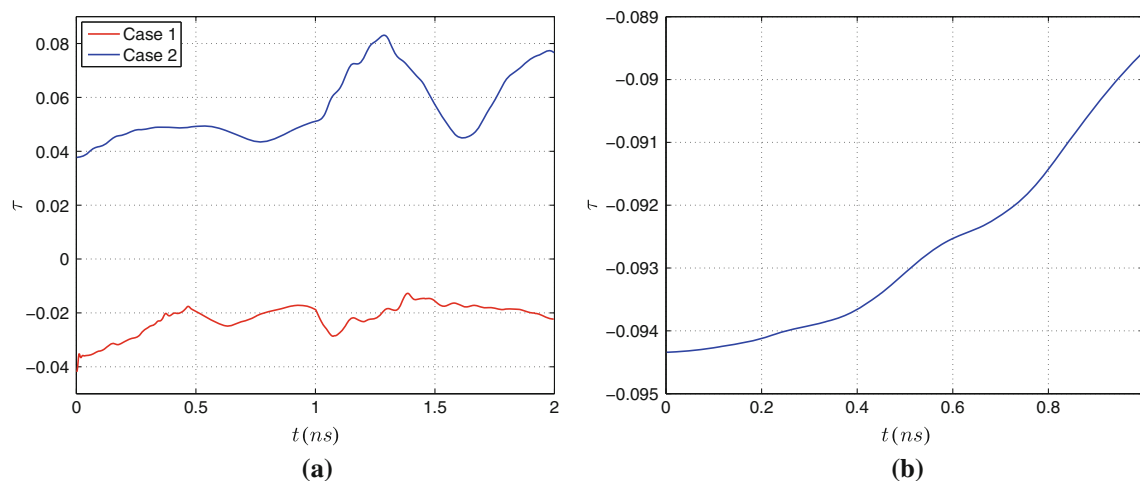


**Fig. 18** Evolution of average dimensionless temperature $\tau$ for **(a)** annulus and **(b)** circular geometries (color online)

## 5 Conclusions

We have developed a numerical formulation of the phase-field model based on the IGA for SMAs. The formulation permits straightforward treatment of fourth-order spatial differential terms representing domain walls in SMAs, without the use of mixed finite element formulation or non-conforming elements. Several numerical examples have been presented with evolution under dynamic loadings. We validated the IGA implementation with the results of quadratic Lagrange basis element using the commercial finite element software with maximum error less than 1 %. The *h*- and *k*-refinement studies suggested that the maximum error with coarsest mesh (quadratic $32^2$) is 2 % with respect to most refined quartic $128^2$ indicating that the simulations can be conducted even on the coarsest mesh with good accuracy. The dynamic loading studies are in agreement with previously published literature on mixed formulations using commercial software and available experimental results.

The developed framework should prove to be useful in the study of thermo-mechanical dynamics of a realistic 3D SMA specimen under complex loadings.

# References

1. Ahluwalia R, Lookman T, Saxena A (2006) Dynamic strain loading of cubic to tetragonal martensites. Acta Mater 54(8):2109–2120
2. Ahluwalia R, Lookman T, Saxena A, Shenoy S (2004) Pattern formation in ferroelastic transitions. Phase Trans 77(5–7):457–467
3. Auricchio F, Da Veiga LB, Hughes TJR, Reali A, Sangalli G (2010) Isogeometric collocation methods. Math Models Methods Appl Sci 20(11):2075–2107
4. Auricchio F, da Veiga LB, Hughes T, Reali A, Sangalli G (2012) Isogeometric collocation for elastostatics and explicit dynamics. Comput Methods Appl Mech Eng 249252:2–14
5. Auricchio F, da Veiga LB, Kiendl J, Lovadina C, Reali A (2013) Locking-free isogeometric collocation methods for spatial Timoshenko rods. Comput Methods Appl Mech Eng 263:113–126
6. Bazilevs Y, Calo V, Cottrell J, Evans J, Hughes T, Lipton S, Scott M, Sederberg T (2010) Isogeometric analysis using T-splines. Comput Methods Appl Mech Eng 199(58):229–263
7. Bhattacharya K (2003) Microstructure of martensite: why it forms and how it gives rise to the shape-memory effect. Oxford University Press, Oxford
8. Borden MJ, Verhoosel CV, Scott MA, Hughes TJ, Landis CM (2012) A phase-field description of dynamic brittle fracture. Comput Methods Appl Mech Eng 217:77–95
9. Bouville M, Ahluwalia R (2008) Microstructure and mechanical properties of constrained shape memory alloy nanograins and nanowires. Acta Mater 56(14):3558–3567
10. Chen L (2002) Phase-field models for microstructure evolution. Annu Rev Mater Res 32(1):113–140
11. Chen L, Shen J (1998) Applications of semi-implicit Fourier-spectral method to phase field equations. Comput Phys Commun 108(2):147–158
12. Comsol multiphysics finite element analysis software. http://www.comsol.com
13. Cottrell J, Hughes T, Reali A (2007) Studies of refinement and continuity in isogeometric structural analysis. Comput Methods Appl Mech Eng 196(4144):4160–4183
14. Cottrell J, Reali A, Bazilevs Y, Hughes T (2006) Isogeometric analysis of structural vibrations. Comput Methods Appl Mech Eng 195(4143):5257–5296
15. Cottrell JA, Hughes TJR, Bazilevs Y (2009) Isogeometric analysis: toward integration of CAD and FEA. Wiley, New York
16. De Lorenzis L, Temizer I, Wriggers P, Zavarise G (2011) A large deformation frictional contact formulation using NURBS-based isogeometric analysis. Int J Numer Methods Eng 87(13):1278–1300
17. Dedè L, Borden MJ, Hughes TJ (2012) Isogeometric analysis for topology optimization with a phase field model. Arch Comput Methods Eng 19(3):427–465
18. Dhote R, Gomez H, Melnik R, Zu J (2013) Isogeometric analysis of coupled thermo-mechanical phase-field models for shape memory alloys using distributed computing. Procedia Comput Sci 18:1068–1076
19. Dhote R, Melnik R, Zu J (2012) Dynamic thermo-mechanical coupling and size effects in finite shape memory alloy nanostructures. Comput Mater Sci 63:105–117
20. Elguedj T, Bazilevs Y, Calo V, Hughes T (2008) B and F projection methods for nearly incompressible linear and non-linear elasticity and plasticity using higher-order NURBS elements. Comput Methods Appl Mech Eng 197(3340):2732–2762
21. Falk F (1980) Model free energy, mechanics, and thermodynamics of shape memory alloys. Acta Metall 28(12):1773–1780
22. Gadaj S, Nowacki W, Pieczyska E (2002) Temperature evolution in deformed shape memory alloy. Infrared Phys Technol 43(3–5):151–155
23. Gomez H, Calo V, Bazilevs Y, Hughes T (2008) Isogeometric analysis of the Cahn–Hillard phase-field model. Comput Methods Appl Mech Eng 197(49–50):4333–4352
24. Gomez H, Hughes TJ, Nogueira X, Calo VM (2010) Isogeometric analysis of the isothermal Navier–Stokes–Korteweg equations. Comput Methods Appl Mech Eng 199(2528):1828–1840
25. Gomez H, Nogueira X (2012) An unconditionally energy-stable method for the phase field crystal equation. Comput Methods Appl Mech Eng 249252:52–61
26. Gomez H, Paris J (2011) Numerical simulation of asymptotic states of the damped Kuramoto–Sivashinsky equation. Phys Rev E 83:046702
27. Greer J, Bertozzi A, Sapiro G (2006) Fourth order partial differential equations on general geometries. J Comput Phys 216(1):216–246
28. Hughes T, Cottrell J, Bazilevs Y (2005) Isogeometric analysis: CAD, finite elements, NURBS, exact geometry and mesh refinement. Comput Methods Appl Mech Eng 194(3941):4135–4195
29. Kiendl J, Bazilevs Y, Hsu MC, Wchner R, Bletzinger KU (2010) The bending strip method for isogeometric analysis of Kirchhoff–Love shell structures comprised of multiple patches. Comput Methods Appl Mech Eng 199(3740):2403–2416
30. Kim JY, Youn SK (2012) Isogeometric contact analysis using mortar method. Int J Numer Methods Eng 89(12):1559–1581
31. Levitas V, Preston D (2002) Three-dimensional Landau theory for multivariant stress-induced martensitic phase transformations. I. Austenite ↔ martensite. Phys Rev B 66(134206):1–9
32. Liu J, Dede L, Evans JA, Borden MJ, Hughes TJ (2013) Isogeometric analysis of the advective Cahn–Hilliard equation: spinodal decomposition under shear flow. J Comput Phys 242:321–350
33. Mamivand M, Zaeem MA, El Kadiri H (2013) A review on phase field modeling of martensitic phase transformation. Comput Mater Sci 77:304–311
34. Melnik R, Roberts A, Thomas KA (2000) Computing dynamics of copper-based SMA via center manifold reduction models. Comput Mater Sci 18:255–268
35. Ng N, Ahluwalia R, Srolovitz D (2012) Domain patterns in free-standing nanoferroelectrics. Acta Mater 60(8):3632–3642
36. Pieczyska E, Tobushi H (2010) Temperature evolution in shape memory alloy during loading in various conditions. In 10th international conference on quantitative infrared thermography, p 5–10
37. Provatas N, Elder K (2010) Phase-field methods in materials science and engineering. Wiley-VCH, Weinheim
38. Raknes S, Deng X, Bazilevs Y, Benson D, Mathisen K, Kvamsdal T (2013) Isogeometric rotation-free bending-stabilized cables: statics, dynamics, bending strips and coupling with shells. Comput Methods Appl Mech Eng 263:127–143
39. Salje E, Buckley A, Van Tendeloo G, Ishibashi Y, Nord G (1998) Needle twins and right-angled twins in minerals: comparison between experiment and theory. Am Mineral 83(7–8):811–822
40. Schillinger D, Ded L, Scott MA, Evans JA, Borden MJ, Rank E, Hughes TJ (2012) An isogeometric design-through-

analysis methodology based on adaptive hierarchical refinement of NURBS, immersed boundary methods, and T-spline CAD surfaces. Comput Methods Appl Mech Eng 249252:116–150

41. Scott M, Simpson R, Evans J, Lipton S, Bordas S, Hughes T, Sederberg T (2013) Isogeometric boundary element analysis using unstructured T-splines. Comput Methods Appl Mech Eng 254:197–221

42. Steinbach I (2009) Phase-field models in materials science. Model Simul Mater Sci Eng 17:073001–073031

43. Steinbach I, Shchyglo O (2011) Phase-field modelling of microstructure evolution in solids: perspectives and challenges. Curr Opin Solid State Mater Sci 15(3):87–92

44. Vilanova G, Colominas I, Gomez H (2013) Capillary networks in tumor angiogenesis: from discrete endothelial cells to phase-field averaged descriptions via isogeometric analysis. Int J Numer Methods Biomed Eng 29(10):1015–1037

45. Wang L, Melnik R (2007) Model reduction applied to square to rectangular martensitic transformations using proper orthogonal decomposition. Appl Numer Math 57(5):510–520

46. Yamanaka A, Takaki T, Tomita Y (2008) Elastoplastic phase-field simulation of self- and plastic accommodations in cubic tetragonal martensitic transformation. Mater Sci Eng A 491(1):378–384